nature astronomy

Article

https://doi.org/10.1038/s41550-024-02300-0

Separate effects of irradiation and impacts on lunar metallic iron formation observed in Chang'e-5 samples

Received: 3 March 2023

Accepted: 16 May 2024

Published online: 20 June 2024

Check for updates

Laiquan Shen[1,7] ✉, Rui Zhao[1,2,7], Chao Chang[1,2,7], Jihao Yu[1,2], Dongdong Xiao[1] ✉, Haiyang Bai[1,2,3] ✉, Zhigang Zou[4,5], Mengfei Yang[4,6] & Weihua Wang[1,3,4]

Nanophase iron particles ($npFe^0$) are generated on the surface of airless bodies by space weathering and can alter surficial optical properties substantially. However, the details of their formation pathways are still unclear. Here we use impact glasses returned from the Moon by Chang'e-5 to distinguish the relative contributions of solar wind irradiation and (micro)meteorites impacts to the production of different-sized $npFe^0$. We show that solar wind irradiation can solely produce small $npFe^0$, via implantation of solar wind ions into the topmost grain surfaces. On the other hand, (micro)meteorite impacts produce directly large $npFe^0$ in melts, through impact-triggered disproportionation reaction or thermal decomposition. These nanoparticles are also capable to further coalesce into micrometre-sized Fe^0 particles during impacts. These findings can help in predicting the space-weathering behaviour of regions exposed to different space environments.

Space weathering modifies the exposed surfaces of airless bodies such as asteroids, Mercury and the Moon over time by the bombardment of (micro)meteorites, solar wind and cosmic rays[1–6]. The nanophase metallic iron particles ($npFe^0$) accumulated during space weathering are responsible for the alterations of optical spectra of airless bodies. The $npFe^0$ with different sizes exhibit distinct optical effects[5–8]: the small $npFe^0$ (<10 nm) cause reddening of visible reflectance, while the relatively large $npFe^0$ (>40 nm) only darken reflectance across all wavelengths, and the $npFe^0$ with intermediate sizes cause reddening and darkening of visible and near-infrared reflectance. Understanding the precise nature of the formation of $npFe^0$ with different sizes is the central issue in studies of space weathering, since it constrains the behaviour and timescales of spectral alterations on regions exposed to different space environments[3,4,9–13].

Despite extensive studies, the origins of $npFe^0$ remain a controversial issue[4,5,12,13]. The ongoing controversy is the respective roles of the two main agents: micrometeorite impacts versus solar wind irradiation. Both agents are proposed to produce $npFe^0$ via multiple underlying mechanisms[5], such as impact-induced vapour deposition[1,4,14,15] or disproportionation reaction[11,16,17], and solar wind-associated hydrogen reduction under melting[18] or ion sputtering deposition[4]. Generally, vapour deposition is considered as the main mechanism based on the findings of small $npFe^0$ in vapour-deposited rims of Apollo samples[4,5,14,15]. A popular viewpoint is then established that vapour deposition is the primary origin of small $npFe^0$, and large $npFe^0$ come from later aggregation of pre-existing small $npFe^0$ during impact-induced remelting[1,5,13–15]. However, spectroscopic measurements of lunar swirls and asteroids suggest the possible independent production of small $npFe^0$ and large $npFe^0$ (refs. 13,19,20), and the reddening effects induced by small $npFe^0$ are also found to be closely associated with solar wind flux[20–24]. The lack of consensus on the respective contributions of solar wind irradiation and micrometeorite impacts substantially impedes the understanding of space-weathering

[1]Institute of Physics, Chinese Academy of Sciences, Beijing, China. [2]Center of Materials Science and Optoelectronics Engineering, University of Chinese Academy of Sciences, Beijing, China. [3]Songshan Lake Materials Laboratory, Dongguan, China. [4]Qian Xuesen Laboratory of Space Technology, China Academy of Space Technology, Beijing, China. [5]College of Engineering and Applied Sciences, Nanjing University, Nanjing, China. [6]China Academy of Space Technology, Beijing, China. [7]These authors contributed equally: Laiquan Shen, Rui Zhao, Chao Chang. ✉e-mail: shenlaiquan@iphy.ac.cn; dongdongxiao@iphy.ac.cn; hybai@iphy.ac.cn

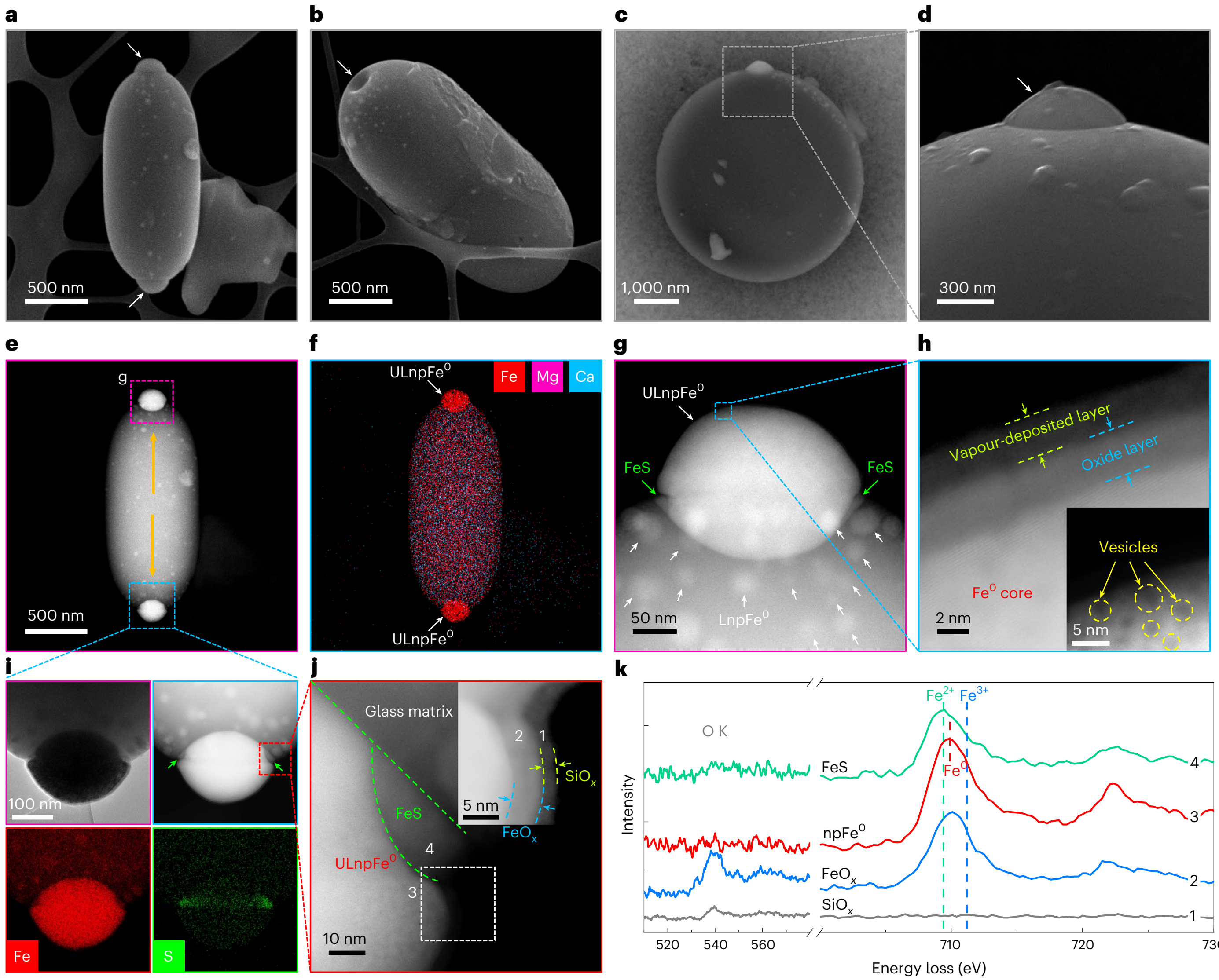

Fig. 1 | Characterizations of ULnpFe⁰ on extremities of impact glasses. a, SE image of a glass ellipsoid with hemispherical bulges on both extremities. The white arrows mark the bulges. **b**, SE image of a glass ellipsoid with a pit on the extremity. The white arrow marks the pit. **c**, BSE image of a glass oblate spheroid with a bulge on one extremity. **d**, Close-up SE image of the marked extremity in **c**. **e**, HAADF-STEM image of the ellipsoid in **a**. The white arrow marks the bulge. The bulges, appearing as bright dots, are globules protruding from the two extremities of the glass ellipsoid. The orange arrows mark the elongation direction of the ellipsoid. **f**, EDS mapping of the ellipsoid in **e**, showing the protruded globules are metallic iron particles with a diameter of ~240 nm (ULnpFe^0). **g**, Close-up HAADF image of the top extremity in **e**. Many discrete Fe^0 particles of approximately tens of nanometres (LnpFe^0) marked by white arrows gather around the ULnpFe^0. Two FeS fractions appearing as fractured notches are found at the interface between the ULnpFe^0 and the host glass, as marked by green arrows. **h**, HAADF image of the surface of ULnpFe^0 in **g**. A uniform double-layer rim coats the ULnpFe^0. The outmost layer is vapour-deposited SiO_x without any npFe^0. The inner layer is an oxide layer of iron. The inset is the image with adjusted contrast of the same region, showing many vesicles on ULnpFe^0, as marked by the yellow circles. **i**, Close-up TEM, STEM and EDS mapping of the bottom extremity in **e**. Same as the top ULnpFe^0, the bottom ULnpFe^0 also has two fractured notches rich in Fe and S, and S is distributed mainly at the interface. **j**, HAADF image of the junction of ULnpFe^0, FeS fraction and glass matrix marked in **i**. The inset is the enlarged image with adjusted contrast of the region marked by the white box, showing the double-layer rim. **k**, EELS spectra of O K edge and Fe $L_{2,3}$ edges for different sampling positions 1–4 marked in **j**.

behaviour under complex space environments[9–13,20–22]. To clarify the controversy over irradiation and impacts, a combined study of the origins of different-sized npFe^0 is urgently required.

The newly returned Chang'e-5 (CE-5) lunar soils provide an opportunity to study the formation of different-sized npFe^0. The CE-5 soils are mature samples collected from higher latitude[25,26] and exhibit obviously higher FeO content than previous lunar samples[12,26]. In this Article, by choosing a series of CE-5 impact glasses as targets, we show that single glass beads can preserve three sizes of npFe^0, including small npFe^0 of approximately several nanometres (SnpFe^0), large npFe^0 of approximately tens of nanometres (LnpFe^0) and ultralarge npFe^0 reaching up to approximately hundreds of nanometres (ULnpFe^0). The SnpFe^0 and (U)LnpFe^0 are further confirmed as the respective products of irradiation and impacts, highlighting that solar wind and micrometeorites both play important but distinct roles in space weathering.

Results

Concentration of (U)LnpFe^0 towards impact glasses extremities

Impact glasses are products of fast cooling of melted ejecta triggered by hypervelocity impacts[27,28]. Here, diverse CE-5 impact glasses with oblong shapes are collected, as shown in Fig. 1a–d and Supplementary Fig. 1. The rotation feature results from non-axisymmetric rotations of melted impact ejecta[29,30], where the associated centrifugal forces

 https://doi.org/10.1038/s41550-024-02300-0

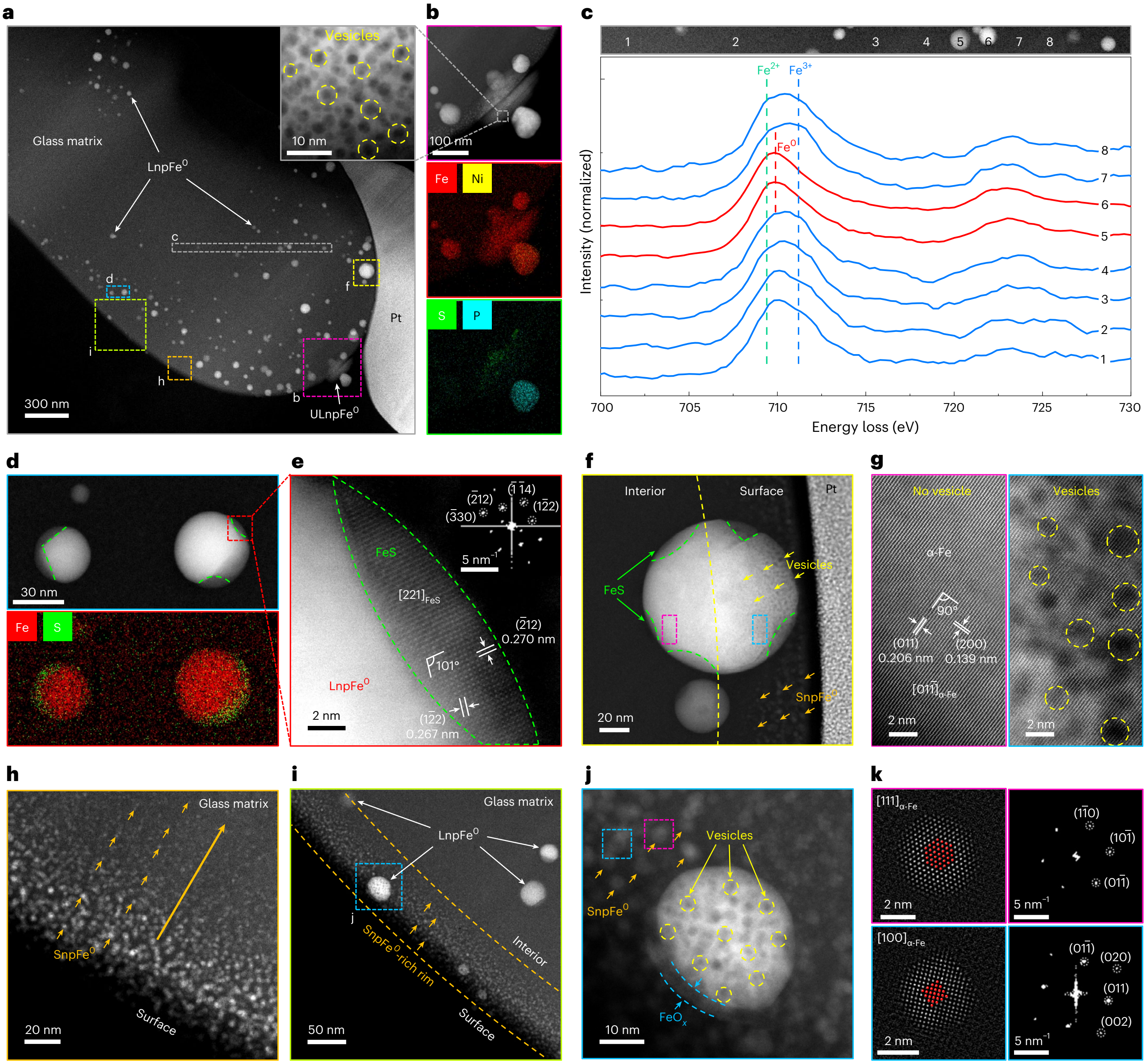

Fig. 2 | Characterizations of volume-correlated LnpFe^0 and surface-correlated SnpFe^0 in an impact glass. a, HAADF image of the FIB section of a glass ellipsoid. Many LnpFe^0 appearing as bright dots distribute randomly inside the glass matrix. **b**, Close-up HAADF image and EDS mapping of the extremity marked by the pink box in **a**. There is a hemispherical and a globular ULnpFe^0 adhering to the extremity of the ellipsoid. The enlarged image in the inset in **a** shows abundant vesicles on ULnpFe^0. EDS mapping shows that the glass extremity is enriched in S, and the globular ULnpFe^0 is composed of Fe, Ni and P. **c**, HAADF image (top) of the region marked by the grey rectangle in **a** and corresponding EELS spectra (bottom) of Fe $L_{2,3}$ edges for different sampling positions 1–8. **d**, HAADF image (top) and EDS mapping (bottom) of two typical LnpFe^0 of the region marked by the cyan rectangle in **a**. The HAADF image shows the whole globular inclusions containing bright parts (Fe^0) and dark parts (FeS), as indicated by the green lines. **e**, Close-up HAADF image of the marked region in **d** and the fast Fourier transform (FFT) pattern along the [221] zone axis of troilite of the FeS fraction. **f**, HAADF image of a typical LnpFe^0 near the glass surface marked by the yellow box in **a**. Five FeS notches are found on the LnpFe^0. The right part of the LnpFe^0 near the surface has abundant vesicles, but the left part has no vesicle. The yellow line indicates the interface of area with and without vesicles. The yellow arrows mark the typical vesicles gradually decreasing in size. **g**, Comparison of the left and right part of the LnpFe^0 marked in **f**. **h**, Close-up HAADF image of the surface region marked by the orange box in **a**. Abundant SnpFe^0 appearing as bright small dots fill the glass surface. The large orange arrow marks the depth direction. The small orange arrows mark the typical SnpFe^0 gradually decreasing in size. **i**, Close-up HAADF image of the surface region marked by the green box in **a**. The densely distributed SnpFe^0 form a SnpFe^0-rich rim with the thickness of ~70 nm, as indicated by the two orange lines. **j**, Close-up HAADF image of the surface region marked by the box in **i**. The LnpFe^0 in the SnpFe^0-rich rim has abundant vesicles. A shell of oxide of iron appears only on the outward-facing part of the LnpFe^0. **k**, HAADF images and corresponding FFT patterns along the [111] and [100] zone axis of α-Fe of two typical SnpFe^0 marked by the two boxes in **j**.

will elongate spherical viscous melts to oblate spheroids, ellipsoids or dumbbells. Notably, unlike previous glass beads with smooth surfaces[28,30], glass beads here are found frequently to carry hemispherical bulges on extremities (Fig. 1a,d and Supplementary Fig. 1), where the falling out of a bulge can leave a pit (Fig. 1b). The high-angle annular dark-field scanning transmission electron microscope (HAADF-STEM)

https://doi.org/10.1038/s41550-024-02300-0

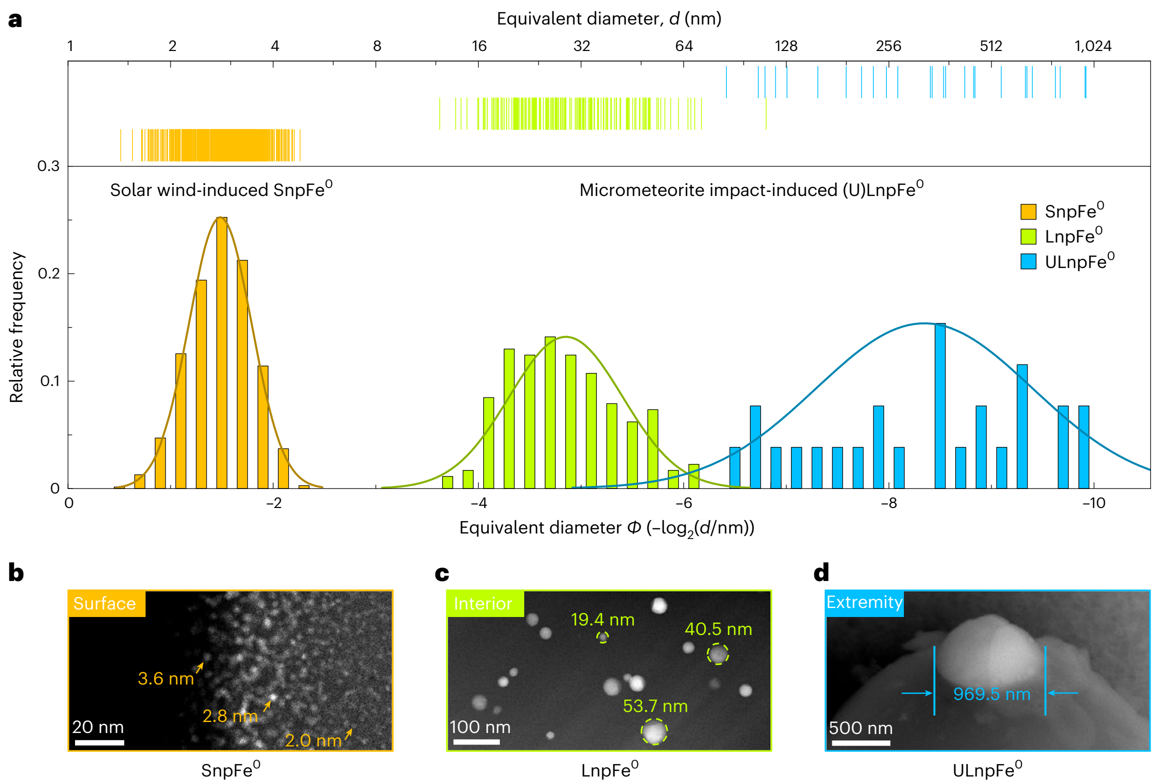

Fig. 3 | Size distributions of the three different types of npFe^0. a, Size statistics of small npFe^0 (SnpFe^0), large npFe^0 (LnpFe^0) and ultralarge npFe^0 (ULnpFe^0), respectively. Colour lines are Gauss fittings of the size distributions. The sizes of SnpFe^0 are concentrated in a narrow range of 1–5 nm with an average of 3 nm. The sizes of LnpFe^0 and ULnpFe^0 vary widely, ranging from 12 to 112 nm and 85 to 970 nm, with an average of 31 nm and 411 nm, respectively. The 701 SnpFe^0 dots and 177 LnpFe^0 dots are collected from Fig. 2h and Fig. 2a, respectively. The ULnpFe^0 are collected from extremities of 22 rotational glass beads. **b**–**d**, Typical SnpFe^0, LnpFe^0 and ULnpFe^0 with different sizes and spatial distribution characteristics. The surface-correlated SnpFe^0 are densely dispersed beneath the grain surface and gradually decrease in size from 5 to 1 nm along the depth direction (**b**). The volume-correlated LnpFe^0 with sizes of approximately tens of nanometres are randomly dispersed in the interior of the glass matrix (**c**). The ULnpFe^0 protruding from the extremity of an impact glass can be as large as ~1 µm (**d**).

image in Fig. 1e shows that the bulges on both extremities are globules protruding from the host glass beads. Energy-dispersive spectroscopy (EDS) mapping in Fig. 1f shows that the protruded globules are metallic iron, namely ULnpFe^0 with diameters up to approximately hundreds of nanometres. Enlarged images identify that there are also many discrete Fe^0 particles of approximately tens of nanometres (LnpFe^0) gathering around the ULnpFe^0 (Fig. 1g and Supplementary Fig. 2c). The concentration of ULnpFe^0 and LnpFe^0 towards extremities of impact glasses indicates that (U)LnpFe^0 must have migrated in the melted ejecta driven by the rotational centrifugal forces, and their formation therefore occurs before the solidification of the impact glass beads[29,30].

Careful observations find that ULnpFe^0 are not always pure iron. Some of the ULnpFe^0 can contain part of iron sulfide, which is identified as troilite by EDS (Fig. 1i and Supplementary Fig. 3c,f) and lattice fringes (Supplementary Fig. 3d). The FeS fractions appear as fractured notches at the interface between ULnpFe^0 and the host glass (Fig. 1g,i and Supplementary Fig. 3). Moreover, surfaces of ULnpFe^0 and glass beads are widely found to be coated by a uniform amorphous rim consisting of Si and O (Supplementary Figs. 2d–f and 3g,h). The distinct compositions indicate that the rim is a vapour-deposited layer generated by micrometeorite impacts[14,15]. It should be noted that, different from previous reports of Apollo samples[1,5,15], the observed deposited layers are much thinner and do not contain any npFe^0 (see also Supplementary Fig. 4 for mineral grains), implying the minor contribution of vapour deposition to produce npFe^0 here. Besides the outmost deposited SiO_x rims, some ULnpFe^0 exhibit double-layer rims (Fig. 1h,j and Supplementary Fig. 3g). Electron energy loss spectroscopy (EELS) spectra of the inner layer in Fig. 1k detect the signal of O and mixed Fe^{2+} and Fe^{3+}, suggesting an oxide layer of iron[31]. This oxide layer forms a shell covering the ULnpFe^0 core, as a typical result of lunar secondary oxidations[31,32].

Volume-correlated LnpFe^0 and their impact origin

To further study the origins of npFe^0, a section of the glass ellipsoid in Supplementary Fig. 1e is prepared by focused ion beam (FIB) technology. As shown in Fig. 2a, there are numerous LnpFe^0 distributing randomly inside the glass matrix. The analyses of iron valence states show that the Fe $L_{2,3}$ spectra of LnpFe^0 exhibit a typical Fe^0 L_3 peak position (~709.9 eV) (positions 5 and 6 in Fig. 2c), whereas the matrix regions do not simply show Fe^{2+} peak (~709.4 eV) but give a broad asymmetric peak with a position between the Fe^{2+} and the Fe^{3+} peak (~711.2 eV), indicating the coexistence of Fe^{2+} and Fe^{3+} (Fig. 2c and Supplementary Fig. 6). The contents of Fe^{3+} are variable for different positions and trend to increase near LnpFe^0 (positions 4 and 7 in Fig. 2c), suggesting the association of Fe^{3+} and Fe^0. Since the interior LnpFe^0 are confirmed as Fe^0 without core–shell structures like that only observed on grain surfaces in Figs. 1h,j and 2j, the occurrence of secondary oxidation or degassing of reductive gases can be ruled out in the interior glass matrix[16,31,32]. Therefore, the associated coexistence of LnpFe^0 and Fe^{3+} indicates an alternative process of disproportionation reaction of Fe^{2+} in impact-generated melts[11,16,17].

Besides those typical LnpFe^0 completely composed of metallic iron, some (U)LnpFe^0 are found to contain S- or P-bearing fractions. Similar to the S distribution in Fig. 1i, there is an enrichment of S and P around the extremity of the ellipsoid section (Fig. 2b).

https://doi.org/10.1038/s41550-024-02300-0

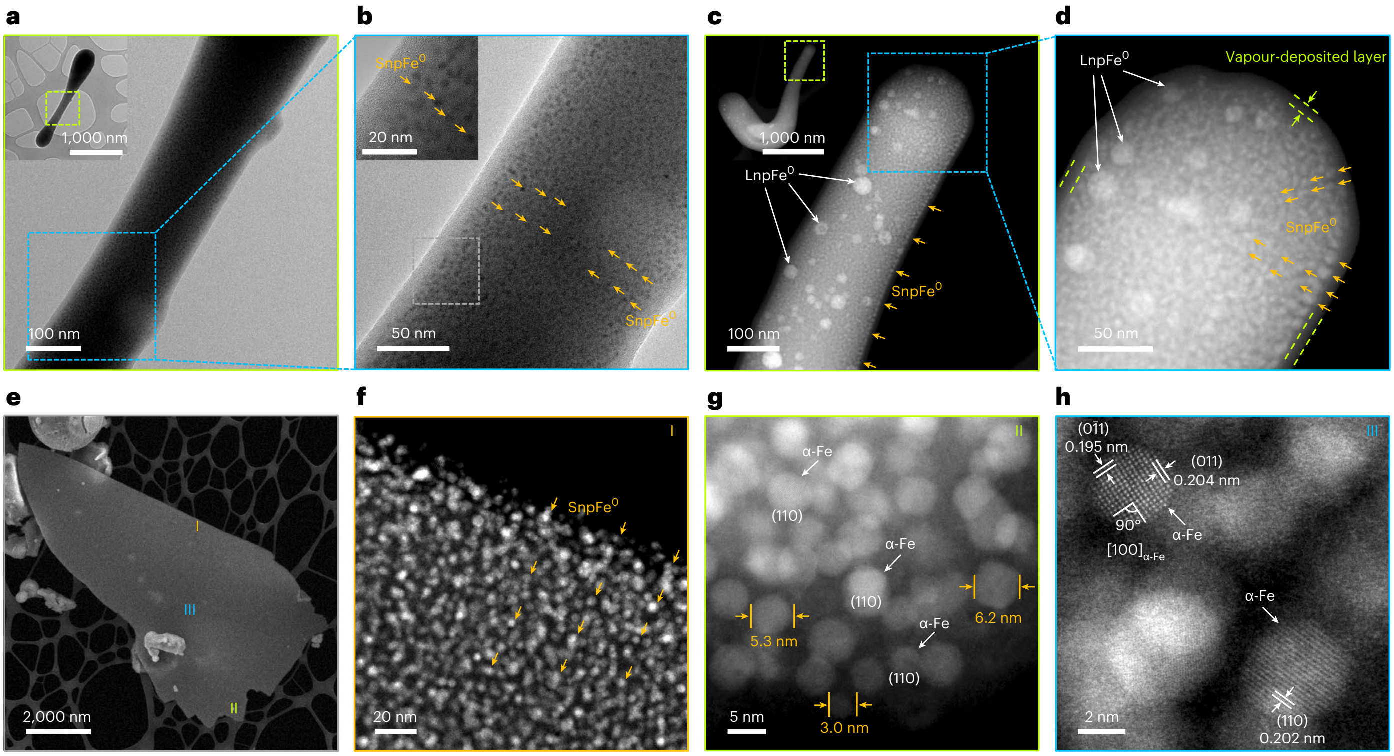

Fig. 4 | Abundant $SnpFe^0$ throughout tiny glass grains. a,**b**, TEM images of the thin central part (**a** and **b**) of a tiny glass dumbbell (inset in **a**). Pervasive $SnpFe^0$ appearing as dark dots fill up the dumbbell. The orange arrows mark the typical $SnpFe^0$. **c**,**d**, HAADF images of the thin shank (**c** and **d**) of a pipe-shaped glass (inset in **c**). Dense $SnpFe^0$ and discrete $LnpFe^0$ appearing as bright dots are distributed throughout the glass grain. A clear vapour-deposited layer without any $npFe^0$ coats the grain surface. **e**–**h**, HAADF images of an ultrathin glass shard with sharp fractured edges. The glass shard (**e**) is full of massive $SnpFe^0$ (**f**–**h**). The $SnpFe^0$ are confirmed as α-Fe according to the lattice fringes (**g** and **h**).

These S- and P-bearing parts probably arise from the original tiny troilite and schreibersite grains produced by shock-induced dissemination[27,33]. Moreover, numerous $LnpFe^0$ are shown to have FeS notches (Fig. 2d,f and Supplementary Fig. 5), which are confirmed as troilite (Fig. 2e). These observations indicate that troilite debris could indeed be mixed into impact-generated melts by shock-induced dissemination[27]. The mixed troilite grains in high-temperature melts can be thermally decomposed into metallic iron and sulfur gas escaping to space[33–35]. The sulfur loss of troilite grains to different degrees finally produces globular inclusions from pure $LnpFe^0$ to irregular intergrowths of Fe^0 with varying fractions of FeS (ref. 34).

Surface-correlated $SnpFe^0$ and their irradiation origin

The lunar soils exposed to space will undergo solar wind irradiation. The typical results of irradiation damages are vesicular textures found on grain surfaces[31,36–38]. As shown in Figs. 1h and 2a and Supplementary Fig. 7a,d, the surface-exposed $ULnpFe^0$ contain abundant vesicles with the size ranging from 1 to 5 nm. Similarly, vesicles appear on the near-surface $LnpFe^0$ but gradually decrease in size and finally disappear with the depth increasing (Fig. 2f,g and Supplementary Fig. 7g). These observations indicate that the vesicles form on $(U)LnpFe^0$ through outside irradiation processes and only appear within the penetration depth of solar wind ions.

By careful checking of the glass section, another kind of $npFe^0$ associated with the observed vesicles, that is, small $npFe^0$ with sizes of approximately several nanometres ($SnpFe^0$), is discovered. As shown in Fig. 2h and Supplementary Fig. 8, there are abundant $SnpFe^0$ appearing as bright small dots filling the ellipsoid surface and forming a uniform $SnpFe^0$-rich rim (Fig. 2i). The surface-correlated $SnpFe^0$ are also confirmed as metallic iron by EELS (Supplementary Fig. 7n) and α-Fe by lattice fringes (Fig. 2k). The consistent compositions of the $SnpFe^0$-rich rim and the interior glass matrix (Supplementary Fig. 8g) exclude the deposition origin of the observed $SnpFe^0$ (refs. 14,15,39). It is further noted that the appearance of $SnpFe^0$ and vesicles is closely associated. Along the ellipsoid surface, all $LnpFe^0$ in the $SnpFe^0$-rich rim have vesicles, and those outside the rim have no vesicles (Fig. 2f,i,j and Supplementary Fig. 7). Similar to the distribution of vesicles, along the depth direction, $SnpFe^0$ gradually decrease in size and abundance, and will finally disappear when the depth exceeds ~120 nm (Fig. 2h and Supplementary Fig. 8), consistent with the reported penetration depth of solar wind[39–41]. These findings strongly indicate that $SnpFe^0$ and vesicles share a common origin of solar wind irradiation, and their gradient distribution feature is attributed to the decreasing amount of implanted solar wind ions with the increase of depth. Further studies of different types of mineral grain also show that implantation of solar wind into the topmost grain surfaces can damage the mineral structures and meanwhile produce widespread surface-correlated $SnpFe^0$ in the irradiated rims (Supplementary Figs. 9–11). These observations together suggest that solar wind irradiation rather than vapour deposition is the main driver of surface-correlated $SnpFe^0$ in CE-5 grains.

Size distribution of iron particles

Given that size of $npFe^0$ is an important parameter in affecting optical spectra wavelengths[5–8,12], the size distributions of $SnpFe^0$, $LnpFe^0$ and $ULnpFe^0$ are statistically analysed. As shown in Fig. 3a, the sizes of $SnpFe^0$ are usually smaller than 5 nm with an average of 3 nm. As comparison, the $LnpFe^0$ and $ULnpFe^0$ have a wide size distribution, and their sizes vary substantially from 12 to 112 nm with an average of 31 nm, and from 85 to 970 nm with an average of 411 nm, respectively. In contrast to the volume-correlated $LnpFe^0$ formed in impact-generated melts (Fig. 3c), the irradiation-derived $SnpFe^0$ are surface correlated (Fig. 3b), and correspondingly, the much smaller and more homogeneous sizes

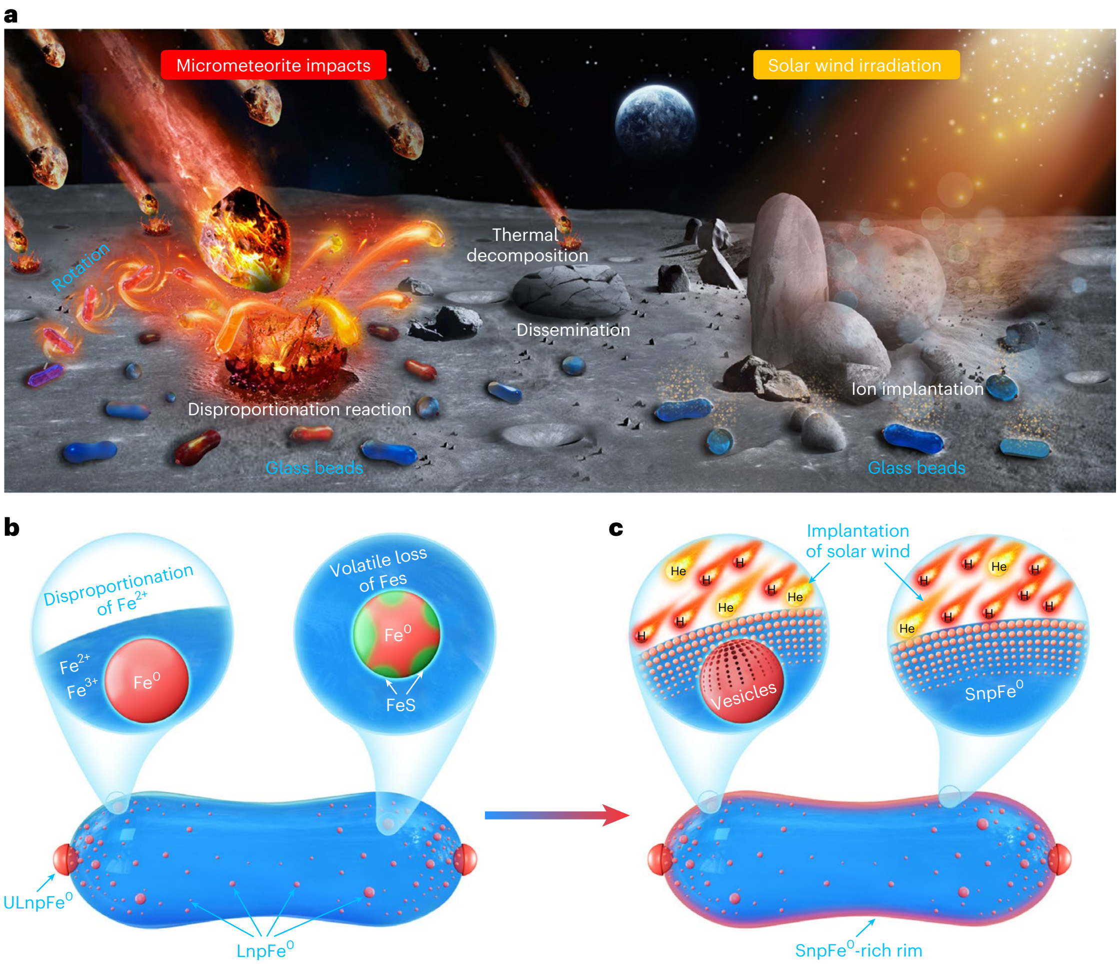

Fig. 5 | Schematic of origins of npFe^0. **a**, Respective effects of (micro)meteorite impacts and solar wind irradiation. Impacts trigger the disproportion reaction of Fe^{2+}, synchronously producing Fe^0 and Fe^{3+} in melts. Impacts also mix some FeS fractions produced by shock-induced dissemination in melts where the S loss of FeS contributes to Fe^0. The rotation of melted impact ejecta results in rotational glass beads to record the produced Fe^0. The exposed lunar grains suffer from solar wind irradiation. The implanted solar wind ions reduce Fe-bearing grains to produce Fe^0. **b**, An impact glass dumbbell with native LnpFe^0 and ULnpFe^0. The impact-derived Fe^0 can easily merge into LnpFe^0 in melts, and then coalesce into ULnpFe^0 protruding out from the extremities driven by rotations. The produced (U)LnpFe^0 are finally frozen with the quenching of glass beads. **c**, An irradiated impact glass dumbbell with newly formed SnpFe^0. The implantation of solar wind into the topmost grain surface causes vesicle damages on the near-surface pre-existing LnpFe^0. Abundant SnpFe^0 are produced within the penetration depth of solar wind, resulting in a SnpFe^0-rich rim.

of SnpFe^0 should owe to the slower diffusion and growth of metallic iron in solids. In melts, the produced metallic iron can nucleate quickly and grow up into LnpFe^0, and further coalesce into ULnpFe^0, resulting in ultralarge-sized Fe^0 particles reaching up to ~1 µm (Fig. 3d).

Since SnpFe^0 are attributed to solar wind irradiation, one can expect that, if the size of an irradiated grain is comparable to twice the penetration depth of solar wind (~240 nm), solar wind would implant throughout the grain and, thus, result in SnpFe^0 filling up the whole grain. This is exactly the case observed in tiny impact glasses in Fig. 4. Both the tiny dumbbell-shaped and pipe-shaped grains in Fig. 4a–d are found to be full of dense SnpFe^0. In contrast, the vapour-deposited layers coating the grain surfaces are free of any npFe^0 (Fig. 4a–d and Supplementary Fig. 12). Figure 4e–h shows an ultrathin glass shard as a fragment of fractured glass grain. Sharp fractured edges of the shard suggest that it does not undergo any remelting after formation (Supplementary Fig. 13a–c). Abundant SnpFe^0 are observed throughout the shard (Fig. 4e–h and Supplementary Fig. 13d–i). Such phenomena can be also found in the ultrathin olivine shard (Supplementary Fig. 14), where dense SnpFe^0 are embedded in the crystalline matrix. These observations further support that solar wind irradiation is capable to solely produce abundant SnpFe^0, even if there are no accompanied impacts or remelting processes[42]. The revealed tiny grains full of SnpFe^0 are also coincident with the fact that npFe^0 abundance and soil maturity increase with decreasing grain size[2,12].

Discussion

We show a schematic diagram in Fig. 5 to systematically illustrate the respective roles of (micro)meteorite impacts and solar wind irradiation in dominating the formation of npFe^0. The produced npFe^0 with different sizes and distribution features can be accumulated in an exposed impact glass. On the basis of precise analyses of microstructures, compositions and valence states, we clearly reveal that the formation of large and small npFe^0 with distinct optical effects is governed by independent processes, corresponding to (micro)meteorite impacts and solar wind irradiation, respectively.

Our findings highlight the multiple mechanisms to form npFe^0 and clarify the respective contributions of impacts and irradiation in producing npFe^0, which are important to understand space-weathering effects under different space environments[5,9–13,20–24]. Generally, impacts are thought to produce small npFe^0 through vapour depositions[1,3,5]. However, the prevalent npFe^0-free vapour-deposited layers of CE-5 grains indicate the minor contribution of impacts in producing small

$npFe^0$ in CE-5 samples. The reason is probably that impacts at the CE-5 landing site are relatively gentle and not enough to vapour and dissociate FeO as supported by recent simulated experiments[43]. Such a gentle impact environment results in much thinner vapour-deposited layers with the lack of metallic elements such as Fe, Mg, Ti, Al and Ca (refs. 5,14,15,44,45). Alternatively, we reveal that impacts can produce large $npFe^0$ via two distinctive mechanisms: disproportionation reaction and thermal decomposition. The non-equilibrium high-temperature and high-pressure condition generated by impacts is capable to trigger a disproportionation reaction of Fe^{2+}, synchronously producing Fe^{3+} and Fe^0 (refs. 11,16,17). In addition, the observed irregular intergrowths of Fe^0 and FeS fractions indicate impact-induced thermal decomposition[46] and preferential loss of volatiles of Fe-bearing fractions mixed in melts, which highlights the role of impacts in changing both optical properties and sulfur abundance of airless bodies[6,47].

Besides impacts, we demonstrate that solar wind irradiation also plays an important role in space weathering via the production of small $npFe^0$ beneath the grain surfaces. Combining with our experimental observations, the space-weathering mechanism of solar wind is neither through sputtering deposition of solar wind ions[4] nor by hydrogen reduction under impact-induced melting[18], but probability via the reduction effects during the implantation of solar wind hydrogen and helium[42]. Solar wind is mainly composed of H^+ (~95.4%) and He^+ (~4.6%). Irradiation simulated experiments show that both He^+ and H^+ irradiation can produce small $npFe^0$ in the irradiation-damaged regions[42,48,49]. Energetic solar wind ions will disrupt the microstructures of grains and break the Fe–O bonds, leaving dangling bonds. Metallic iron could be reduced in this process, while abundant H^+ are free to react with the dangling bonds, creating OH/H_2O to promote the reduction process[42]. Latest studies have indeed identified solar wind-derived OH/H_2O on grain surfaces[39,40,50], where the content of water or hydrogen decreases with depth[39,40], consistent with the observed gradient distributions of small $npFe^0$. Moreover, the amount of time required to form small $npFe^0$ by solar wind irradiation can be estimated on the basis of exposure age calculated from solar flare track densities (Supplementary Fig. 11)[51]. The estimated rate of 10^5–10^6 years is consistent with previous laboratory irradiation experiments that give a timescale of 10^4–10^6 years[4,52]. However, given that the high-energy solar flare particles can penetrate much deeper than the solar wind ions, the actual solar wind irradiation time should be shorter than 10^5–10^6 years[40,51]. In fact, recent studies of impact gardening also indicate a rather short direct exposure time of 10^3–10^4 years for the top few grain layers[53,54]. It is worthwhile to determine the accurate formation rate of small $npFe^0$ and take account of gardening effects in future studies.

Since solar wind is the main mechanism for small $npFe^0$ formation, the FeO-rich basalts at the CE-5 landing site can thus efficiently accumulate small $npFe^0$ by solar wind irradiation, resulting in the mature CE-5 lunar soils[12,23,26]. Namely, even though the CE-5 lunar soils have less agglutinate glass content due to the gentle impact environment[12,26,45], the soils can still reach high maturity owing to the solar wind-dominated space weathering. Additionally, the solar wind origin of small $npFe^0$ could also explain a series of solar wind flux-dependent space-weathering effects in spectroscopic observations[13], from the timescale of space weathering[13,21] to spatial variation of spectral properties on the lunar surface[22,23].

Furthermore, the revealed independent growth of large and small $npFe^0$ is fundamentally different from the conventional view acknowledging the formation of large $npFe^0$ as the aggregation of small $npFe^0$ (refs. 1,5,13,15). This finding is crucial for the interpretation and prediction of spectroscopic observations of airless bodies. For example, the independent growth mechanism may account for the formation of lunar swirls that are generally observed by remote sensing measurements[13,19,20]. The lunar swirls are always associated with local magnetic anomaly, at which the solar wind ions are greatly deflected by magnetic fields and, thus, solar wind-derived small $npFe^0$ is inhibited, resulting in reduced soil maturity[20]. In contrast, impacts at lunar swirls are not obviously affected, leading to the normal abundance of large $npFe^0$ (refs. 13,24).

Strictly speaking, although micrometeorite impacts and solar wind irradiation can produce $npFe^0$ independently, they are not two competing or unrelated processes. In fact, they are two collaborative processes to promote space weathering. On the one hand, when micrometeorites impact and melt the irradiated grains, the pre-existing small $npFe^0$ derived by solar wind irradiation could aggregate into part of large $npFe^0$. On the other hand, impacts can break larger grains into finer grains[5,27]. The finer grains with increased specific surface areas can therefore accumulate small $npFe^0$ more efficiently via solar wind irradiation, resulting in the increase of soil maturity[2,16]. The clarification of the specific roles of micrometeorites and solar wind in space weathering, along with a comprehensive understanding of origins of $npFe^0$, could improve our knowledge of how space weathering modifies the surfaces of airless bodies and, meanwhile, provide implications for interpreting the spectral alterations of airless bodies that experience different weathering processes.

Methods

Samples

The CE-5 lunar samples (CE5C0400) allocated by the China National Space Administration were used in this study. These samples scooped from the lunar surfaces were fine soil powders. The samples are securely stored within a glove box shielded by a continuous supply of dry high-purity nitrogen gas (N_2>99.9999%, H_2O <0.1 ppm, O_2<0.1 ppm). Subsequently, a measured quantity of soils is extracted from these samples within the glove box for each experiment.

Scanning electron microscopy analyses

We examined morphologies and compositions of a series of soil particles using a Thermo Scientific Quattro S field emission scanning electron microscope equipped with an EDS (Bruker XFlash6|30) detector. The soils were directly fixed on adhesive carbon-conductive tap carbon foils or carbon-coated copper holders for scanning electron microscopy observations. An accelerating voltage of 5–15 kV and an electron beam current of 7–14 pA were used for the secondary electron (SE) imaging, whereas the back-scattered electron (BSE) imaging and EDS measurements were performed at an accelerating voltage of 15–20 kV and an electron beam current of 50–120 pA.

TEM analyses

Transmission electron microscopy (TEM) analyses including high-resolution TEM, HAADF-STEM and bright-field STEM imaging were performed on an aberration-corrected JEOL-ARM200F electron microscope operated at 200 kV. Double EDS detectors are equipped to the microscope. The HAADF-STEM images are sensitive to atomic number and, therefore, give fractions with different compositions varied contrast. Especially, Fe^0 particles exhibit bright dots in HAADF-STEM images. The chemical compositions of different micro regions were determined by EDS in HAADF-STEM mode. To reduce the background noise of STEM images, the raw images in Fig. 2k and Supplementary Fig. 13i were filtered by using the average background subtraction filtering method.

The TEM characterizations use two different kinds of specimen. The first kind is fine lunar particles that were directly fixed on carbon-coated copper grids without any other preparation. The second kind is specific electron-transparent sections of glass particles of interest, prepared by FIB cutting using a Talos F200S TEM (Thermo Fisher Scientific). The position recorded for FIB cutting was initially deposited with Pt for protection. We cut the specific thin sections from the particle by a 30 kV Ga^+ ion beam in the FIB system. The sections were next extracted and mounted onto TEM copper grids. After that, we used low ion beam voltage during the section thinning process.

The sections were thinned to about 100 nm using a 10 kV Ga^+ ion beam and were finally cleaned using a 5 kV Ga^+ beam at 40–80 pA.

EELS analyses

The EELS analyses were conducted using a Gatan Continuum S 1077 spectrometer installed in the TEM described above with a dispersion of 0.3 eV per channel and collection semi-angle of 100 mrad. The EELS spectra were collected in dual EELS mode. The acquisition time was no more than 0.05 s per pixel to prevent any beam damage. For the unnormalized spectra, the largest possible region of interest with the same pixel size was selected to enhance signal to noise and make a reasonable comparison. The spectra have been background subtracted using a power law function and Fourier ratio deconvoluted using the associated low-loss spectra from the same specimen area. All the EELS data processing tasks were conducted in the Gatan Microscope Suite software (version 3.50).

Data availability

All data supporting this study are presented in the paper and its Supplementary Information. Source data for Figs. 1–4 are available via figshare at https://doi.org/10.6084/m9.figshare.25683804 (ref. 55).

References

1. Pieters, C. M. et al. Space weathering on airless bodies: resolving a mystery with lunar samples. *Meteorit. Planet. Sci.* **35**, 1101–1107 (2000).
2. Taylor, L. A., Pieters, C. M., Keller, L. P., Morris, R. V. & McKay, D. S. Lunar mare soils: space weathering and the major effects of surface-correlated nanophase Fe. *J. Geophys. Res. Planets* **106**, 27985–27999 (2001).
3. Sasaki, S., Nakamura, K., Hamabe, Y., Kurahashi, E. & Hiroi, T. Production of iron nanoparticles by laser irradiation in a simulation of lunar-like space weathering. *Nature* **410**, 555–557 (2001).
4. Hapke, B. Space weathering from Mercury to the asteroid belt. *J. Geophys. Res. Planets* **106**, 10039–10073 (2001).
5. Pieters, C. M. & Noble, S. K. Space weathering on airless bodies. *J. Geophys. Res. Planets* **121**, 1865–1884 (2016).
6. Noguchi, T. et al. Incipient space weathering observed on the surface of Itokawa dust particles. *Science* **333**, 1121–1125 (2011).
7. Lucey, P. G. & Riner, M. A. The optical effects of small iron particles that darken but do not redden: evidence of intense space weathering on Mercury. *Icarus* **212**, 451–462 (2011).
8. Noble, S. K., Pieters, C. M. & Keller, L. P. An experimental approach to understanding the optical effects of space weathering. *Icarus* **192**, 629–642 (2007).
9. Chapman, C. R. Space weathering of asteroid surfaces. *Annu. Rev. Earth Planet. Sci.* **32**, 539–567 (2004).
10. Pieters, C. M. et al. Distinctive space weathering on Vesta from regolith mixing processes. *Nature* **491**, 79–82 (2012).
11. Li, C. et al. Impact-driven disproportionation origin of nanophase iron particles in Chang'e-5 lunar soil sample. *Nat. Astron.* **6**, 1156–1162 (2022).
12. Lu, X. J. et al. Mature lunar soils from Fe-rich and young mare basalts in the Chang'e-5 regolith samples. *Nat. Astron.* **7**, 142–151 (2022).
13. Tai Udovicic, C. J., Costello, E. S., Ghent, R. R. & Edwards, C. S. New constraints on the lunar optical space weathering rate. *Geophys. Res. Lett.* **48**, e2020GL092198 (2021).
14. Keller, L. P. & McKay, D. S. Discovery of vapor deposits in the lunar regolith. *Science* **261**, 1305–1307 (1993).
15. Keller, L. P. & McKay, D. S. The nature and origin of rims on lunar soil grains. *Geochim. Cosmochim. Acta* **61**, 2331–2341 (1997).
16. Xian, H. Y. et al. Ubiquitous and progressively increasing ferric iron content on the lunar surfaces revealed by the Chang'e-5 sample. *Nat. Astron.* **7**, 280–286 (2023).
17. Bindi, L., Shim, S. H., Sharp, T. G. & Xie, X. D. Evidence for the charge disproportionation of iron in extraterrestrial bridgmanite. *Sci. Adv.* **6**, eaay7893 (2020).
18. Housley, R. M., Grant, R. W. & Paton, N. E. Origin and characteristics of excess Fe metal in lunar glass welded aggregates. *Geochim. Cosmoschim. Acta* **3**, 2737–2749 (1973).
19. Blewett, D. T., Denevi, B. W., Cahill, J. T. S. & Klima, R. L. Near-UV and near-IR reflectance studies of lunar swirls: implications for nanosize iron content and the nature of anomalous space weathering. *Icarus* **364**, 114472 (2021).
20. Glotch, T. D. et al. Formation of lunar swirls by magnetic field standoff of the solar wind. *Nat. Commun.* **6**, 6189 (2015).
21. Vernazza, P., Binzel, R. P., Rossi, A., Fulchignoni, M. & Birlan, M. Solar wind as the origin of rapid reddening of asteroid surfaces. *Nature* **458**, 993–995 (2009).
22. Sim, C. K., Kim, S. S., Lucey, P. G., Garrick-Bethell, I. & Choi, Y. J. Asymmetric space weathering on lunar crater walls. *Geophys. Res. Lett.* **44**, 11273–11281 (2017).
23. Hemingway, D. J., Garrick-Bethell, I. & Kreslavsky, M. A. Latitudinal variation in spectral properties of the lunar maria and implications for space weathering. *Icarus* **261**, 66–79 (2015).
24. Trang, D. & Lucey, P. G. Improved space weathering maps of the lunar surface through radiative transfer modeling of Kaguya multiband imager data. *Icarus* **321**, 307–323 (2019).
25. Li, Q. L. et al. Two billion-year-old volcanism on the Moon from Chang'e-5 basalts. *Nature* **600**, 54–58 (2021).
26. Li, C. L. et al. Characteristics of the lunar samples returned by the Chang'E-5 mission. *Natl Sci. Rev.* **9**, nwab188 (2022).
27. Heiken, G. H., Vaniman, D. T. & French, B. M. *Lunar Sourcebook: A User's Guide to the Moon* 1–721 (Cambridge Univ. Press, 1991).
28. Zellner, N. E. B. Lunar impact glasses: probing the Moon's surface and constraining its impact history. *J. Geophys. Res. Planets* **124**, 2686–2702 (2019).
29. Bastin, J. A. Rotating lunar globules. *Nature* **283**, 108–108 (1980).
30. Pugh, M. J. Rotation of lunar dumbbell-shaped globules during formation. *Nature* **237**, 158–159 (1972).
31. Burgess, K. D. & Stroud, R. M. Coordinated nanoscale compositional and oxidation state measurements of lunar space-weathered material. *J. Geophys. Res. Planets* **123**, 2022–2037 (2018).
32. Thompson, M. S., Zega, T. J., Becerra, P., Keane, J. T. & Byrne, S. The oxidation state of nanophase Fe particles in lunar soil: implications for space weathering. *Meteorit. Planet. Sci.* **51**, 1082–1095 (2016).
33. Brett, R. Reduction of mare basalts by sulfur loss. *Geochim. Cosmochim. Acta* **40**, 997–1004 (1976).
34. Hu, G. L., Dam-Johansen, K., Wedel, S. & Hansen, J. P. Decomposition and oxidation of pyrite. *Prog. Energy Combust. Sci.* **32**, 295–314 (2006).
35. Zolensky, M. E. et al. Mineralogy and petrology of comet 81P/Wild 2 nucleus samples. *Science* **314**, 1735–1739 (2006).
36. Li, A. et al. Taking advantage of glass: capturing and retaining of the helium gas on the moon. *Mater. Futures* **1**, 035101 (2022).
37. Bradley, J. P. et al. Detection of solar wind-produced water in irradiated rims on silicate minerals. *Proc. Natl Acad. Sci. USA* **111**, 1732–1735 (2014).
38. Krishan, K. Ordering of voids and gas bubbles in radiation environments. *Radiat. Eit.* **66**, 121–155 (1982).
39. Zhou, C. J. et al. Chang'E-5 samples reveal high water content in lunar minerals. *Nat. Commun.* **13**, 5336 (2022).
40. Xu, Y. C. et al. High abundance of solar wind-derived water in lunar soils from the middle latitude. *Proc. Natl Acad. Sci. USA* **119**, e2214395119 (2022).
41. Bibring, J. P. et al. Ultrathin amorphous coatings on lunar dust grains. *Science* **175**, 753–755 (1972).

42. Kuhlman, K. R., Sridharan, K. & Kvit, A. Simulation of solar wind space weathering in orthopyroxene. *Planet. Space Sci.* **115**, 110–114 (2015).
43. Weber, I. et al. Space weathering by simulated micrometeorite bombardment on natural olivine and pyroxene: a coordinated IR and TEM study. *Earth Planet. Sci. Lett.* **530**, 115884 (2020).
44. Zhang, S. L. & Keller, L. P. Space weathering effects in lunar soils: the roles of surface exposure time and bulk chemical composition. In *42nd Lunar and Planetary Science Conference* No. JSC-CN-22819 (2011).
45. Zhao, R. et al. Diverse glasses revealed from Chang'E-5 lunar regolith. *Natl Sci. Rev.* **10**, nwad079 (2023).
46. Guo, Z. et al. Nanophase iron particles derived from fayalitic olivine decomposition in Chang'E-5 lunar soil: implications for thermal effects during impacts. *Geophys. Res. Lett.* **49**, e2021GL097323 (2022).
47. Matsumoto, T., Harries, D., Langenhorst, F., Miyake, A. & Noguchi, T. Iron whiskers on asteroid Itokawa indicate sulfide destruction by space weathering. *Nat. Commun.* **11**, 1117 (2020).
48. Loeffler, M., Dukes, C. & Baragiola, R. Irradiation of olivine by 4 keV He^+: Simulation of space weathering by the solar wind. *J. Geophys. Res. Planets* **114**, E03003 (2009).
49. Dukes, C. A., Baragiola, R. A. & McFadden, L. A. Surface modification of olivine by H^+ and He^+ bombardment. *J. Geophys. Res. Planets* **104**, 1865–1872 (1999).
50. Liu, Y. et al. Direct measurement of hydroxyl in the lunar regolith and the origin of lunar surface water. *Nat. Geosci.* **5**, 779–782 (2012).
51. Keller, L. P., Berger, E. L., Zhang, S. & Christoffersen, R. Solar energetic particle tracks in lunar samples: a transmission electron microscope calibration and implications for lunar space weathering. *Meteorit. Planet. Sci.* **56**, 1685–1707 (2021).
52. Strazzulla, G. et al. Spectral alteration of the Meteorite Epinal (H5) induced by heavy ion irradiation: a simulation of space weathering effects on near-Earth asteroids. *Icarus* **174**, 31–35 (2005).
53. Costello, E. S., Ghent, R. R., Hirabayashi, M. & Lucey, P. G. Impact gardening as a constraint on the age, source, and evolution of ice on Mercury and the Moon. *J. Geophys. Res. Planets* **125**, e2019JE006172 (2020).
54. Costello, E. S., Ghent, R. R. & Lucey, P. G. Secondary impact burial and excavation gardening on the Moon and the depth to ice in permanent shadow. *J. Geophys. Res. Planets* **126**, e2021JE006933 (2021).
55. Shen, L. & Chang, C. Distinguishing the effects of irradiation and impacts on lunar metallic iron formation. *figshare* https://doi.org/10.6084/m9.figshare.25683804 (2024).

Acknowledgements

We are indebted to the China National Space Administration (CNSA) for providing the lunar samples. We thank all the staff of China's CE-5 project for their brilliant work returning lunar samples. This work was supported by the National Natural Science Foundation of China (T2322029, 52301225, 52192600, 52001220, 11790291 and 61888102), the Strategic Priority Research Program of the Chinese Academy of Sciences (XDB30000000), the Special Research Assistant Funding Program of the Chinese Academy of Sciences and Guangdong Major Project of Basic and Applied Basic Research, China (2019B030302010).

Author contributions

W.W., H.B., M.Y. and Z.Z. led the project. H.B. and L.S. supervised the research. L.S., R.Z., C.C., H.B. and W.W. conceived this work and wrote the manuscript. L.S. designed the experiments and performed the SEM measurements. D.X. and L.S performed the STEM measurements. L.S., R.Z. and C.C. analysed the experimental data. J.Y. assisted in data collection. All authors contributed to comment on the manuscript writing and the result discussions.

Competing interests

The authors declare no competing interests.

Additional information

Supplementary information The online version contains supplementary material available at https://doi.org/10.1038/s41550-024-02300-0.

Correspondence and requests for materials should be addressed to Laiquan Shen, Dongdong Xiao or Haiyang Bai.

Peer review information *Nature Astronomy* thanks Zongcheng Ling and the other, anonymous, reviewer(s) for their contribution to the peer review of this work.